

LCS Tool : A Computational Platform for Lagrangian Coherent Structures

K. Onu¹, F. Huhn², and G. Haller²

¹Mechanical Engineering, McGill University, Montreal, Canada.

²Institute of Mechanical Systems, ETH Zurich, Switzerland.

June 16, 2014

Abstract

We give an algorithmic introduction to Lagrangian coherent structures (LCSs) using a newly developed computational engine, LCS Tool. LCSs are most repelling, attracting and shearing material lines that form the centerpieces of observed tracer patterns in two-dimensional unsteady dynamical systems. LCS Tool implements the latest geodesic theory of LCSs for two-dimensional flows, uncovering key transport barriers in unsteady flow velocity data as explicit solutions of differential equations. After a review of the underlying theory, we explain the steps and numerical methods used by LCS Tool, and illustrate its capabilities on three unsteady fluid flow examples.

1 Introduction

Lagrangian Coherent Structures (LCSs) are evolving organizing centers of trajectory patterns in non-autonomous dynamical systems [20, 28, 17]. Applications of LCSs include oceanic and atmospheric flows [4, 23], biological transport problems [34, 31, 21], aeronautics [32], celestial mechanics [13], crowd dynamics [1], and aperiodically forced mechanical oscillators [14].

Haller [15] proposed that ridges of the Finite-Time Lyapunov exponent (FTLE) are heuristic indicators of hyperbolic (i.e., repelling- and attracting-type) LCSs. A number of examples indeed support this principle [28]. Equating FTLE ridges with LCSs, however, would create theoretical inconsistencies, as well as false positives and negatives in hyperbolic LCS detection [16, 26]. In addition, the role of the FTLE field in the accurate detection of elliptic (vortex-type) and parabolic (jet-core type) LCSs has remained an open question (but see [3]).

More recent work has focused on an exact mathematical formulation of the properties defining LCSs [16, 11, 18, 19, 5]. In two-dimensional flows, hyperbolic

and parabolic LCSs turn out to be stationary curves of the averaged material shear [12], whereas elliptic LCSs are stationary curves of the averaged strain [19]. These variational formulations lead to explicit solutions for LCSs as null-geodesics of appropriate Lorentzian metrics.

Here we present a simple algorithmic introduction to geodesic LCS detection without details on the the underlying mathematics. We then review the implementation of this approach in a computational engine called LCS Tool¹. This engine is a library of MATLAB functions that extract LCSs from two-dimensional unsteady flows. The examples we present here have been programmed into demonstration scripts.

The list of publicly available software for LCS detection further includes the following packages:

- *MANGEN* [24] calculates FTLE and advects material curves in two-dimensional velocity fields. It also includes a graphical user interface and uses MPI for parallel calculations.
- *LCS MATLAB Kit* [7] calculates the FTLE from velocity datasets. Includes a graphical user interface.
- *Newman* [10] calculates the FTLE in N dimensions. Assists ridge extraction of FTLE fields. Supports analytic- and dataset-based velocity definitions.
- *FlowVC* [29] is a general-purpose LCS platform for two- and three- dimensional datasets. Parallel calculations are supported with OpenMP, CUDA and OpenCL.

These packages primarily target the automated generation of FTLE plots to aid the visual assessment of hyperbolic LCSs in the flow. The purpose of LCS Tool and this article is to provide an all-purpose numerical engine for the geodesic extraction of LCSs as parametrized material curves in unsteady two-dimensional flows, and extend the scope of such extraction to elliptic LCSs.

2 Theory

We consider two-dimensional, finite-time, unsteady velocity fields of the form

$$\dot{x} = v(x, t), \quad x \in U \subset \mathbb{R}^2, \quad t \in [t_-, t_+]. \quad (1)$$

Trajectories of (1) are denoted $x(t; t_0, x_0)$, with $x_0 \in U$ denoting their initial position in the open set U at an initial time $t_0 \in [t_-, t_+]$. The flow map is then defined as

$$F_{t_0}^t(x_0) := x(t; t_0, x_0),$$

mapping initial positions to current positions at time t . The time interval $[t_-, t_+]$ is part of the definition of the finite-time dynamical system (1). This interval

¹LCS Tool is publicly available at: <https://github.com/jeizaw/LCS-Tool>.

may be a time scale of interest or the maximum interval over which velocity data is available from simulations or observations.

The right Cauchy-Green strain tensor associated with the flow map is defined as

$$C_{t_0}^t(x_0) = [\nabla F_{t_0}^t(x_0)]^T \nabla F_{t_0}^t(x_0), \quad (2)$$

measuring Lagrangian strain in the velocity field. This tensor is symmetric and positive definite [33]. We label the eigenvalues and eigenvectors of $C_{t_0}^t(x_0)$ as follows:

$$\begin{aligned} C_{t_0}^t \xi_i &= \lambda_i \xi_i, & 0 < \lambda_1 \leq \lambda_2, & \quad i = 1, 2; \\ |\xi_i| &= 1, & \xi_2 &= \Omega \xi_1, & \quad \Omega = \begin{pmatrix} 0 & -1 \\ 1 & 0 \end{pmatrix}. \end{aligned} \quad (3)$$

2.1 Elliptic LCSs

We seek positions of closed material lines at time t_0 that prevail as coherent Lagrangian vortex boundaries (or *elliptic LCSs*) over a time interval $[t_0, t] \subset [t_-, t_+]$. Haller and Beron-Vera [19] argue that such initial material line positions are closed stationary curves of the averaged strain functional

$$Q(\gamma) = \frac{1}{\sigma} \int_0^\sigma \frac{\sqrt{\langle r'(s), C_{t_0}^t(r(s))r'(s) \rangle}}{\sqrt{\langle r'(s), r'(s) \rangle}} ds,$$

obtained by averaging the tangential strain arising over $[t_0, t]$ along closed material lines parametrized as $r(s)$ with $s \in [0, \sigma]$. Solutions to this variational problem turn out to be closed orbits of one of two parametrized vector-field families

$$\eta_\pm^\lambda = \sqrt{\frac{\lambda_2 - \lambda^2}{\lambda_2 - \lambda_1}} \xi_1 \pm \sqrt{\frac{\lambda^2 - \lambda_1}{\lambda_2 - \lambda_1}} \xi_2, \quad (4)$$

with $\lambda > 0$ playing the role of a parameter. Such closed orbits satisfy the differential equation

$$r' = \eta_\pm^\lambda(r), \quad (5)$$

which coincide with null-geodesics of the Lorentzian metric family $e_\lambda(u, v) = \langle u, [D_{t_0}^t(r) - \lambda^2 I] v \rangle$. For this reason, we refer to the computation of elliptic LCSs as limit cycles of (5) as *geodesic detection of elliptic LCSs*.

Any orbit of (5) turns out to stretch uniformly under the flow map $F_{t_0}^t$. Specifically, any subset of an orbit of (5) increases its arclength precisely by a factor of λ . For this reason, we refer to trajectories of (5) as λ -lines. Following [19], we call the outermost member of a closed family of λ -lines a coherent Lagrangian vortex boundary.

2.2 Hyperbolic LCSs

Next we consider positions of material lines at time t_0 that prevail as most repelling or attracting material lines (or *hyperbolic LCSs*) over a time interval $[t_0, t] \subset [t_-, t_+]$. Farazmand et al. [12] argue that hyperbolic LCSs are stationary curves of the averaged shear functional

$$Q(\gamma) = \frac{1}{\sigma} \int_0^\sigma \frac{\langle r'(s), D_{t_0}^t(r(s))r'(s) \rangle}{\sqrt{\langle r'(s), C_{t_0}^t(r(s))r'(s) \rangle \langle r'(s), r'(s) \rangle}} ds, \quad D_{t_0}^t = \frac{1}{2}[C_{t_0}^t \Omega - \Omega C_{t_0}^t],$$

obtained by averaging the Lagrangian shear arising over $[t_0, t]$ along closed material lines parametrized as $r(s)$ with $s \in [0, \sigma]$. More precisely, hyperbolic LCSs are stationary curves of $Q(\gamma)$ with respect to fixed-endpoint perturbations. We note that parabolic LCSs (Lagrangian jet cores) are also stationary curves of $Q(\gamma)$, but under variable endpoint perturbations (cf. [12]).

Solutions to this variational problem turn out to be orbits of the ξ_1 or ξ_2 eigenvector field. Repelling LCSs (*shrinklines*) are obtained as trajectories of the differential equation

$$r' = \xi_1(r), \tag{6}$$

and attracting LCSs (*stretchlines*) are obtained as trajectories of the differential equation

$$r' = \xi_2(r). \tag{7}$$

Shrinklines and stretchlines coincide with the null-geodesics of the Lorentzian metric $h(u, v) = \langle u, D_{t_0}^t(r)v \rangle$. For this reason, we refer to the computation of hyperbolic LCSs as strongest normally-repelling or normally-attracting orbits of (5) as *geodesic detection of hyperbolic LCSs*.

To compute the normal repulsion of shrinklines, we note that an infinitesimal normal perturbation to a shrinkline γ at its point r grows under the flow map $F_{t_0}^t$ by a factor of $\lambda_2(r)$ in the direction normal to $F_{t_0}^t(\gamma)$. Similarly, small normal perturbations to a stretchline decay by a factor $\lambda_1(r)$ in the direction normal to the evolving stretchline.

1. Define a Cartesian grid for initial conditions of trajectories. Define an auxiliary grid for differentiating with respect to initial conditions.
2. Solve (1) starting from each grid point and auxiliary grid point over the time interval $[t_0, t]$. This gives a discrete approximation to the flow map $F_{t_0}^t(x_0)$.
3. Use finite differencing over the auxiliary grid to compute numerically the derivative of the flow map $DF_{t_0}^t(x_0)$.
4. Compute the Cauchy-Green strain tensor field $C_{t_0}^t(x_0) = (DF_{t_0}^t(x_0))^T DF_{t_0}^t(x_0)$, its eigenvalue field $\lambda_{1,2}(x_0)$, and eigenvector fields $\xi_{1,2}(x_0)$ over the initial condition grid.

Table 1: Algorithm to calculate the invariants of the Cauchy-Green strain tensor field.

3 Numerical methods

Here we describe a step-by-step numerical implementation of the geodesic detection of elliptic and hyperbolic LCSs through the differential equations (5), (6), and (7).

3.1 Computing the invariants of the Cauchy-Green strain tensor

The common first step in calculating elliptic and hyperbolic LCSs is the computation of the Cauchy-Green strain tensor field $C_{t_0}^t(x_0)$, as defined in (2). The function performing this calculation in LCS Tool is `eig_cgStrain`. The main steps executed by this function are enumerated in Table 1, while Table 3.1 summarizes the syntax of `eig_cgStrain`.

The Cartesian grid of initial conditions mentioned in Table 1 is rectangular, with user-defined vertical and horizontal ranges and resolutions. The optimal resolution may be determined by a successive doubling of the initial resolution until convergence of the extracted LCSs is observed visually. If the domain of interest comprises only a few expected LCSs, e.g., one vortex, then a resolution of about 500 grid point along the longest axis usually gives good results. Otherwise, a higher resolution must be chosen.

The auxiliary grid (cf. Table 1) comprises four points placed symmetrically around each point of the Cartesian grid (Figure 1). These points are used to achieve increased accuracy in the finite-difference approximation

$$\nabla F_{t_0}^t(x_0) \approx \begin{pmatrix} \frac{x_1(t; t_0, x_0 + \delta x_1) - x_1(t; t_0, x_0 - \delta x_1)}{2|\delta x_1|} & \frac{x_1(t; t_0, x_0 + \delta x_2) - x_1(t; t_0, x_0 - \delta x_2)}{2|\delta x_2|} \\ \frac{x_2(t; t_0, x_0 + \delta x_1) - x_2(t; t_0, x_0 - \delta x_1)}{2|\delta x_1|} & \frac{x_2(t; t_0, x_0 + \delta x_2) - x_2(t; t_0, x_0 - \delta x_2)}{2|\delta x_2|} \end{pmatrix}$$

[cgEigenvector,cgEigenvalue] = eig_cgStrain(derivative,domain,timespan,resolution)	
derivative	function handle for flow velocity equations
domain	2×2 array to define flow domain
timespan	1×2 array to define flow timespan
resolution	1×2 array to define Cauchy-Green strain main grid resolution
auxGridRelDelta	optional scalar between 0 and 0.5 to specify auxiliary grid spacing. Default is 10^{-2} .
eigenvalueFromMainGrid	optional logical to control whether eigenvalues of Cauchy-Green strain are calculated from main or auxiliary grid. Default is true.
incompressible	optional logical to specify if incompressibility is imposed. Default is false.
odeSolverOptions	optional odeset structure to specify flow map integration parameters

Table 2: Syntax of the function eigcgStrain.

of $\nabla F_{t_0}^t$ at a point x_0 of the Cartesian grid. Here δx_i is a vector of length $|\delta x_i| > 0$ that points from the Cartesian grid-point x_0 in the i^{th} coordinate direction (Figure 1). Computational improvements arising from the use of the auxiliary grid over simply using the nearest points of the main grid were reported in Ref. [11]. Experience suggests an auxiliary grid spacing of 1-10% of the main grid spacing.

The function `eig_cgStrain` of LCS Tool provides the option to calculate Cauchy-Green eigenvectors from the auxiliary grid using eigenvalues calculated from the main grid. We have found that for flows defined analytically, the eigenvalues can reliably be calculated from the main grid. For the flows defined by datasets, using the auxiliary grid for eigenvalue calculations gives better results.

As mentioned above, a typical main grid for the Cauchy-Green strain tensor comprises 500×500 . This means that after the addition of 4 auxiliary grid point around each main grid points, eq. (1) must be integrated over 1.25 million initial conditions.

To avoid excessive computational times in MATLAB, we vectorize (1), i.e., combine its right-hand-side evaluated over each initial points into a single system of equations. The resulting system is composed of independent blocks of two-dimensional first-order ODEs. We then use MATLAB's `ode45` to perform trajectory integration from all grid points simultaneously. This process typically takes five to ten minutes with default error tolerances. A potential drawback of vector form integration is that memory requirements may become excessive at high resolutions. Furthermore, writing the velocity function in vector form is more error-prone than the simpler two-dimensional form.

The Cauchy-Green strain tensor generically admits points singularities, i.e., points where $C_{t_0}^t(x_0)$ has repeated eigenvalues. At these points the eigenvectors $\xi_1(x_0)$ and $\xi_2(x_0)$ are no longer well-defined. This generically arises at a finite

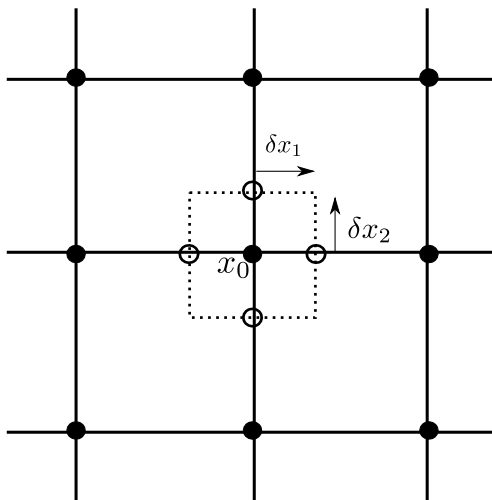


Figure 1: Illustration of the main grid (filled circles) and the auxiliary grid (empty circles) used in the computation of the derivative of the flow map in the definition (2) of the Cauchy–Green strain tensor. The variable `auxGridRelDelta` specifies the grid spacing of the auxiliary grid relative to the main grid spacing.

set of isolated points within the computational domain [9], and hence lie off the computational grid with probability one.

3.1.1 Special case: incompressible velocity fields

Incompressible flows (i.e. those satisfying $\nabla \cdot v = 0$) admit the relationship $\lambda_1(x_0)\lambda_2(x_0) = 1$ at all points of the computational domain [2]. Incompressibility can be computationally imposed by first calculating $\lambda_2(x_0)$, then setting $\lambda_1(x_0) = 1/\lambda_2(x_0)$ and calculating the strain eigenvectors ξ_2 from λ_2 , then ξ_1 from the relationship in (3). Experience shows that computing λ_i in this order gives higher accuracy than in the reverse order [11].

At some grid points, $\lambda_2 < 1$ may occur due to numerical integration errors. By setting the integration tolerances to smaller values, the number of such grid points is reduced. Enforcing $\lambda_2 \geq 1$ everywhere, however, can incur excessive computational cost. To this end, the function `eig_cgStrain` records the number of points with $\lambda_2 < 1$, providing a measure for setting feasible integration tolerances.

3.1.2 Special case: data-defined velocity fields

Velocity fields defined by datasets require pre-processing before they are used in the numerical integration of (1). This requires spatial and temporal interpolation that enables the evaluation of the velocity function at arbitrary points

1. Position Poincare sections in flow domain to specify initial positions of lambda-lines
2. Integrate λ -lines tangent to η_{\pm}^{λ} (see (5).)
3. Calculate Poincare map
4. Find closed orbits for fixed points of the Poincare map
5. Identify outermost closed orbit on each Poincare section

Table 3: Algorithm to calculate elliptic LCSs and coherent Lagrangian vortex boundaries.

in U and at arbitrary times between t_- and t_+ . In section 4.3, we present an ocean dataset example with details of possible interpolation functions.

3.2 Computing elliptic LCSs

As discussed in section (2.1), positions of elliptic LCSs at time t_0 are found as closed orbits of the η_{\pm}^{λ} vector fields defined in (4). We find such orbits by integrating (5) from points of an appropriately chosen section (Poincare section), and evaluating the first return map (Poincaré map) onto this section. A λ -line returning to its starting point is then an elliptic LCS. The outermost member of a family of closed λ -lines (obtained by varying λ) is a coherent Lagrangian vortex boundary [19].

The main steps in calculating elliptic LCSs are enumerated in Table 3 and described in further detail below. The syntax of elliptic LCS functions in LCS Tool is shown in Table 4.

The first step is to define the position of Poincare sections in regions where closed λ -lines are expected based on a visual analysis of the orbit structure of the η_{\pm}^{λ} vector field. The Poincare section is to be oriented such that the first endpoint is close to the center of the expected Lagrangian vortex, and the second endpoint is outside this vortex. There is no automated procedure implemented yet in LCS Tool for the positioning of Poincare sections (see, however, [22] for a recently developed algorithm). Additionally, the number of lambda-lines launched from the Poincaré section, `poincareSection.numPoints`, must be defined. A reasonable default value is 100.

The second step is to integrate the λ -lines starting from the Poincare section to obtain the corresponding Poincare map. Integration of λ -lines is performed using the η_{\pm}^{λ} vector fields defined in (4) over the main grid. The underlying eigenvector fields $\xi_i(x_0)$ have generic but removable orientation discontinuities, which require monitoring and reorientation, as needed. This process is sketched in Table 5 and illustrated in Figure 2. Linear interpolation is used in the interpolation of η_{\pm}^{λ} within a grid element, since using higher-order interpolation would necessitate verifying that there are no orientation discontinuities beyond the

[shearline.etaPos,shearline.etaNeg] = lambda_line(CG Eigenvector,CG Eigenvalue, lambda)	
cgEigenvector	array of Cauchy-Green strain eigenvectors
cgEigenvalue	array of Cauchy-Green strain eigenvalues
lambda	scalar lambda value in Equation (4)
[closedOrbits,orbits] = poincare_closed_orbit_multi(domain,resolution,shearline, PSList)	
domain	array to define flow domain
resolution	1×2 array to define main grid resolution for Cauchy-Green strain tensor
shearline	structure of arrays of η_+^λ and η_-^λ values on main grid
PSList	user-defined structure for Poincare section end-points, number of λ -lines launched from Poincare section, and maximum closed λ -line length
nBisection	optional number of bisection steps to refine zero crossings of Poincare map. Default values: 5.
dThresh	optional threshold to discard discontinuous zero crossings of Poincare map. Default value: 10^{-2} .
odeSolverOptions	optional odeset structure to specify λ -line integration parameters
periodicBc	optional 1×2 logical array to specify periodic boundary conditions. Default is [false,false].

Table 4: Syntax of LCS Tool's elliptic LCS functions.

1. Linearly interpolate vector field orientation at initial position
2. At next position, check whether vector field has rotated by over 90° , if yes, flip the vector field orientation by 180° .
3. Stop integration when λ -line returns to Poincare section, λ -line reaches the domain boundary, or maximum integration length has been reached.

Table 5: Algorithm used for variable time step integration of λ -lines.

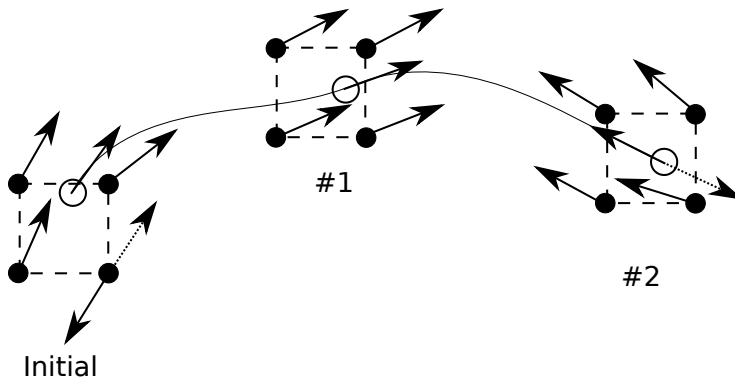


Figure 2: Schematic illustration of the variable-time-step λ -line integration. At the initial point, there is an orientation discontinuity at the lower-right grid point that must be corrected prior to linear interpolation. At point #1, no orientation discontinuities are present. At point #2 all interpolated η_{\pm}^{λ} vectors must be rotated by 180° to match the orientation of the trajectory.

four nearest grid points. We identify orientation discontinuities by checking the inner product of the η_{\pm}^{λ} vectors at adjacent grid points. Rotations exceeding 90° between two such neighboring vectors are classified as orientation discontinuities and are corrected before linear interpolation. When setting the Cauchy-Green strain tensor main grid resolution, one may find it helpful to calculate a histogram of eigenvector-field rotations to ensure that all rotations are well below 90° .

An example of a Poincare map produced from integration of the η_{\pm}^{λ} field is shown in Figure 3. Most orbits will return to the Poincare section and their integration will then be stopped using the ODE event detection function of MATLAB. Some orbits may, however, deviate far from the Poincare section and do not return for any reasonable integration time. To control this behavior, we specify a maximum orbit length, `poincareSection.orbitMaxLength`. In practice, viewing the Poincare section as the radius of a circle and setting the maximum λ -line integration length to twice the circumference gives good results.

In Figure 3, circle markers indicate fixed points of the Poincare map, i.e.,

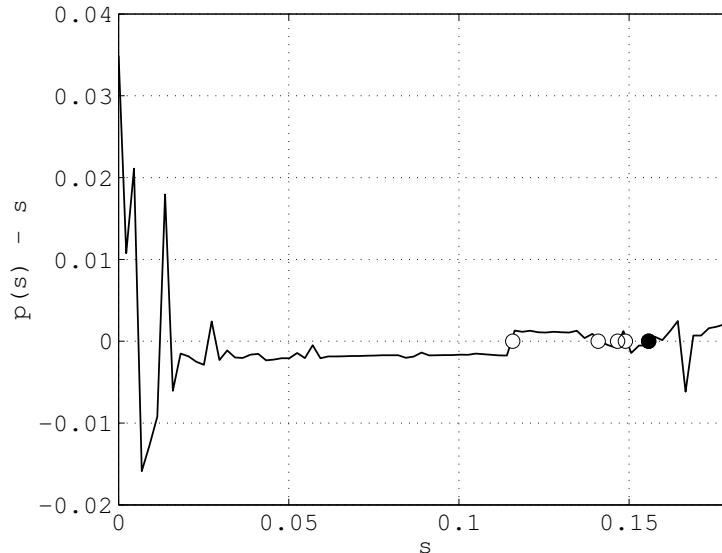


Figure 3: Example of a Poincaré map obtained for an elliptic LCS region. Circle markers indicate closed orbit positions. The filled circle indicates the outermost fixed point of the Poincaré map, marking the intersection of a coherent Lagrangian vortex boundary with the Poincaré section.

points where the distance between the final and the initial point of the orbit $P(s) - s$, is zero. The function `poincare_closed_orbit_multi` performs the computations. As seen in Figure 3, LCS Tool uses a filtering parameter `dThresh` to discard sign changes of $P(s) - s$ that are likely due to numerical sensitivity or a jump discontinuity of the Poincaré map. Specifically, the location of each detected zero crossing is first refined by the bisection method. If after a predetermined number of iterations, `nBisection` (default value 5) the two points around the zero crossing still have absolute values above `dThresh`, the zero crossing is discarded. Once all valid closed λ -lines have been located, the outermost closed λ -orbit associated with every Poincaré section is identified as a coherent Lagrangian vortex boundary.

3.3 Computing hyperbolic LCSs

As discussed in section (2.2), positions of hyperbolic LCSs at time t_0 are found as the strongest repelling orbits of the vector field (6) (repelling LCSs), and strongest attracting orbits of the vector field (7) (attracting LCSs). By repulsion and attraction we mean a property of the LCS (as an evolving material line) under the flow map $F_{t_0}^t$. We identify the strongest repelling shrinklines as those crossing a local maximum of the $\lambda_2(x_0)$ field. Similarly, we identify the strongest attracting stretchlines as those crossing a local minimum of the $\lambda_1(x_0)$ field.

1. Define a local maximization distance.
2. Find all points of the main grid that are local maxima of λ_2 within a circle whose radius is the local maximization distance.
3. Define a maximum shrinkline length
4. Integrate a shrinkline forward and backward according to Equation (6) and using the largest λ_2 local maximum as the initial position. Integrate until the shrinkline has attained the maximum shrinkline length, or until it has reached the domain boundary.
5. Flag any remaining local maxima of λ_2 within the maximization distance of the shrinkline as ineligible initial positions for subsequent shrinklines
6. Continue integrating shrinklines using local maxima of λ_2 as initial positions until no eligible local maxima of λ_2 remain.
7. Remove all shrinkline segments falling within elliptic LCSs.

Table 6: Algorithm to calculate initial positions of repelling LCSs at time t_0 . The algorithm for attracting LCSs is similar.

These local maxima and minima of the appropriate $\lambda_i(x_0)$ eigenvalue field can be thought of as the extensions of the concept of a saddle points to the present finite-time, temporally aperiodic flow setting.

The main steps of our hyperbolic LCS detection algorithm are enumerated in Table 6. The basic function to compute hyperbolic LCSs in LCS Tool is `seed_curves_from_lambda_max`, with its syntax is given in Table 7.

In classical, infinite-time dynamical systems, elliptic and hyperbolic invariant manifolds cannot intersect, as the trajectories in their intersection would then have to follow two different asymptotic behaviors simultaneously. In finite-time dynamical systems, hyperbolic LCSs may well intersect elliptic LCSs, with hyperbolic LCSs continuing to act as cores of mixing patterns observed in the interior of elliptic LCSs. Motivated by convention and for clarity in visualization, however, the default setting of LCS Tool removes hyperbolic LCS segments from the interior of elliptic LCSs. These removed segments can be turned back on demand, as shown in Figure 4.

[curvePosition,curveInitialPosition] = seed_curves_from_lambda_max(distance, cgEigenvalue,cgEigenvector,flowDomain,flowResolution)	
distance	threshold distance for placement of $\lambda_2(x_0)$ maxima
cgEigenvalue	array of Cauchy-Green strain eigenvalues
cgEigenvector	array of Cauchy-Green strain eigenvectors
flowDomain	2×2 array to define flow domain
flowResolution	1×2 array to define Cauchy-Green strain main grid resolution
periodicBc	optional 1×2 logical array to specify periodic boundary conditions. Default is [false,false].
nMaxCurves	optional maximum number of curves (i.e. shrinklines of stretchlines) to generate. Default is numel(cgEigenvalue).
odeSolverOptions	optional odeset structure to specify flow map integration parameters

Table 7: Syntax of the function seed_curves_from_lambda_max

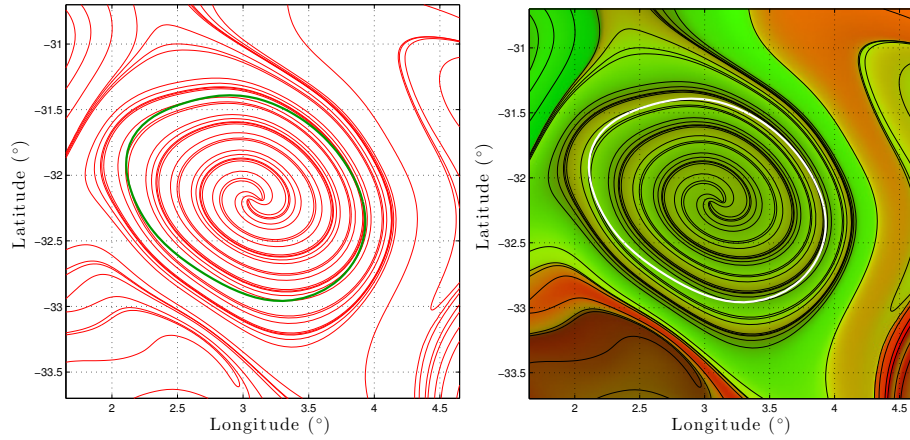


Figure 4: (Left) Elliptic LCS (green) with repelling LCSs (red) continuing into its interior. (Right) Final positions $x(t) = (x_1(t), x_2(t)) = F_{t_0}^t(x_0)$ of tracer particles, with their $x_1(t)$ -position encoded in red and $x_2(t)$ -position encoded in green color. Note the continued impact of the repelling hyperbolic LCSs (black) on tracer patterns inside the elliptic LCS (white).

4 Examples

In this section we present examples of the use of LCS Tool to obtain LCSs in three different examples: a double gyre, a jet, and an oceanic geostrophic flow. All three examples are available as demonstration files in the demo folder of LCS Tool. By executing these scripts, readers can follow LCS Tool computations step-by-step. Additionally, LCS Tool includes scripts to animate the three flows.

4.1 Double gyre

The double gyre is a model for a time-dependent two-gyre system observed in geophysical flows [30]. The model consists of two counter-rotating sinusoidal vortices with a harmonically oscillating line in-between. Lagrangian particle motions satisfy the non-autonomous dynamical system

$$\begin{aligned}\dot{x} &= -\pi A \sin[\pi f(x, t)] \cos(\pi y), \\ \dot{y} &= \pi A \cos[\pi f(x, t)] \sin(\pi y) \frac{\partial f(x, t)}{\partial x}, \\ f(x, t) &= \epsilon \sin(\omega t) x^2 + [1 - 2\epsilon \sin(\omega t)] x.\end{aligned}\tag{8}$$

The MATLAB function describing this model velocity field is given in Listing 1, specifying the right-hand-side of the particle ODE in a way that supports vectorized integration.

```
function derivative_ = derivative(t,x,epsilon,amplitude,omega)
2
  idx1 = 1:2:numel(x)-1;
4  idx2 = 2:2:numel(x);

6  a = epsilon*sin(omega*t);
  b = 1 - 2*epsilon*sin(omega*t);
8  forcing = a*x(idx1).^2 + b*x(idx1);

10 derivative_ = nan(size(x));

12 derivative_(idx1) = -pi*amplitude*sin(pi*forcing).*cos(pi*x(idx2));
  derivative_(idx2) = pi*amplitude*cos(pi*forcing).*sin(pi*x(idx2)).*(2*a*x(idx1)
    + b);
```

Listing 1: Definition of double gyre flow.

In what follows, the parameter values are: $A = 0.1$, $\epsilon = 0.1$, $\omega = \pi/5$. The flow timespan is $t \in [0, 10]$ and the domain is $x \in [0, 2]$, $y \in [0, 1]$. By examining the FTLE field (which is optionally provided by LCS Tool), we position Poincare sections to capture elliptic LCSs. An LCS Tool demo script to perform this operation is given in Listing 2 where two Poincare sections are defined (ll. 18-19). The free stretching parameter λ (Eq. 5) is varied over the range $[0.93, 1.07]$ with increments of 0.01 (ll. 27-28). In a loop (ll. 35-39), closed orbits for all

predefined λ values are computed and the outermost closed orbit is kept as the Lagrangian vortex boundary. In this script, we have chosen small values for the error tolerances of the integration of the Cauchy-Green strain tensor (1.14) and λ -lines (1.26) to facilitate convergence.

```

1  %% Input parameters
   epsilon = .1;
3  amplitude = .1;
   omega = pi/5;
5  domain = [0,2;0,1];
   resolution = [500,250];
7  timespan = [0,10];

9  %% Velocity definition
   IDerivative = @(t,x,~)derivative(t,x,false,epsilon,amplitude,omega);
11 incompressible = true;

13 %% LCS parameters
   cgStrainOdeSolverOptions = odeset('relTol',1e-5);
15

   %% Lambda-lines
17 poincareSection = struct('endPosition', {}, 'numPoints', {}, 'orbitMaxLength', {});
   poincareSection(1).endPosition = [0.55,0.55;0.1,0.1];
19 poincareSection(2).endPosition = [1.53,.45;1.95,0.05];
   [poincareSection.numPoints] = deal(100);
21 nPoincareSection = numel(poincareSection);
   for i = 1:nPoincareSection
23     rOrbit = hypot(diff(poincareSection(i).endPosition(:,1)),diff(poincareSection
       (i).endPosition(:,2)));
       poincareSection(i).orbitMaxLength = 2*(2*pi*rOrbit);
25   end
   lambdaLineOdeSolverOptions = odeset('relTol',1e-6);
27 lambdaStep = 0.01;
   lambdaRange = 0.93:lambdaStep:1.07;
29

   %% Cauchy-Green strain eigenvalues and eigenvectors
31 [cgEigenvector,cgEigenvalue] = eig_cgStrain(IDerivative,domain,resolution,
       timespan,'incompressible',incompressible,'odeSolverOptions',
       cgStrainOdeSolverOptions);

33 %% Lambda-line LCSs

35 for lambda = lambdaRange
   ...
37     closedLambdaLineCandidate = poincare_closed_orbit_multi(domain,
       resolution,shearline,poincareSection,'odeSolverOptions',
       lambdaLineOdeSolverOptions,'showGraph',showGraph);
   ...
39 end

```

Listing 2: Double gyre script for elliptic λ -line LCSs

In Figure 5, the resolution of the Cauchy-Green strain tensor is varied from $[500 \times 250]$ to $[1000 \times 500]$. The location of the outermost closed λ -line changes insignificantly, demonstrating convergence. For all tested resolutions the λ values of the outermost closed orbits are constant. This also suggests that the lowest tested resolution of $[500 \times 250]$ is sufficient to identify the elliptic LCS in this example.

Figure 6 shows the complete picture of elliptic and hyperbolic LCSs of the double gyre at this resolution. Listing 3 lists the corresponding LCS Tool commands. The maximal length of shrinklines and stretchlines, `shrinklineMaxLength` and `stretchlineMaxLength`, is set to 20, a multiple of the domain size, since the hyperbolic LCSs may wind around vortices several times.

As usual, the local maximization distance is set larger for stretchlines than for shrinklines (cf. 1.4 and 19). The purpose of the maximization distance is to obtain spatially separated LCSs and to avoid a dense tangle of lines that basically indicates the same hyperbolic LCS (cf. Table 6, point 5). Setting the local maximization distance for stretchlines larger than for shrinklines allows obtaining a comparable number of stretchlines and shrinklines overall in the flow domain (recall that hyperbolic LCS seed points are discarded if they are within the local maximization distance of an existing hyperbolic LCS.) Shrinklines are locally tangent to ridges of λ_2 maxima, whereas stretchlines are locally normal to these ridges. Setting the local maximization distance of stretchlines and shrinklines equal would therefore produce a greater number of stretchlines than shrinklines overall.

```
% Shrinklines
2 shrinklineMaxLength = 20;
  gridSpace = diff(domain(1,:))/(double(resolution(1))-1);
4 shrinklineLocalMaxDistance = 2*gridSpace;
  strainlineOdeSolverOptions = odeset('relTol',1e-6);
6
% Stretchlines
8 stretchlineMaxLength = 20;
  stretchlineLocalMaxDistance = 10*gridSpace;
10 stretchlineOdeSolverOptions = odeset('relTol',1e-6);

12 %% Hyperbolic shrinkline LCSs
   [shrinklineLcs,shrinklineLcsInitialPosition] = seed_curves_from_lambda_max(
       shrinklineLocalMaxDistance,shrinklineMaxLength,cgEigenvalue(:,2),
       cgEigenvector(:,1:2),domain,resolution,'odeSolverOptions',
       shrinklineOdeSolverOptions);
14 ...
%% Hyperbolic stretchline LCSs
16 [stretchlineLcs,stretchlineLcsInitialPosition] = seed_curves_from_lambda_max(
       stretchlineLocalMaxDistance,stretchlineMaxLength,-cgEigenvalue(:,1),
```



```
cgEigenvector(:,3:4),domain,resolution,'odeSolverOptions',  
stretchlineOdeSolverOptions);
```

```
...
```

Listing 3: Excerpt from demo script to compute hyperbolic LCS for the double gyre flow.

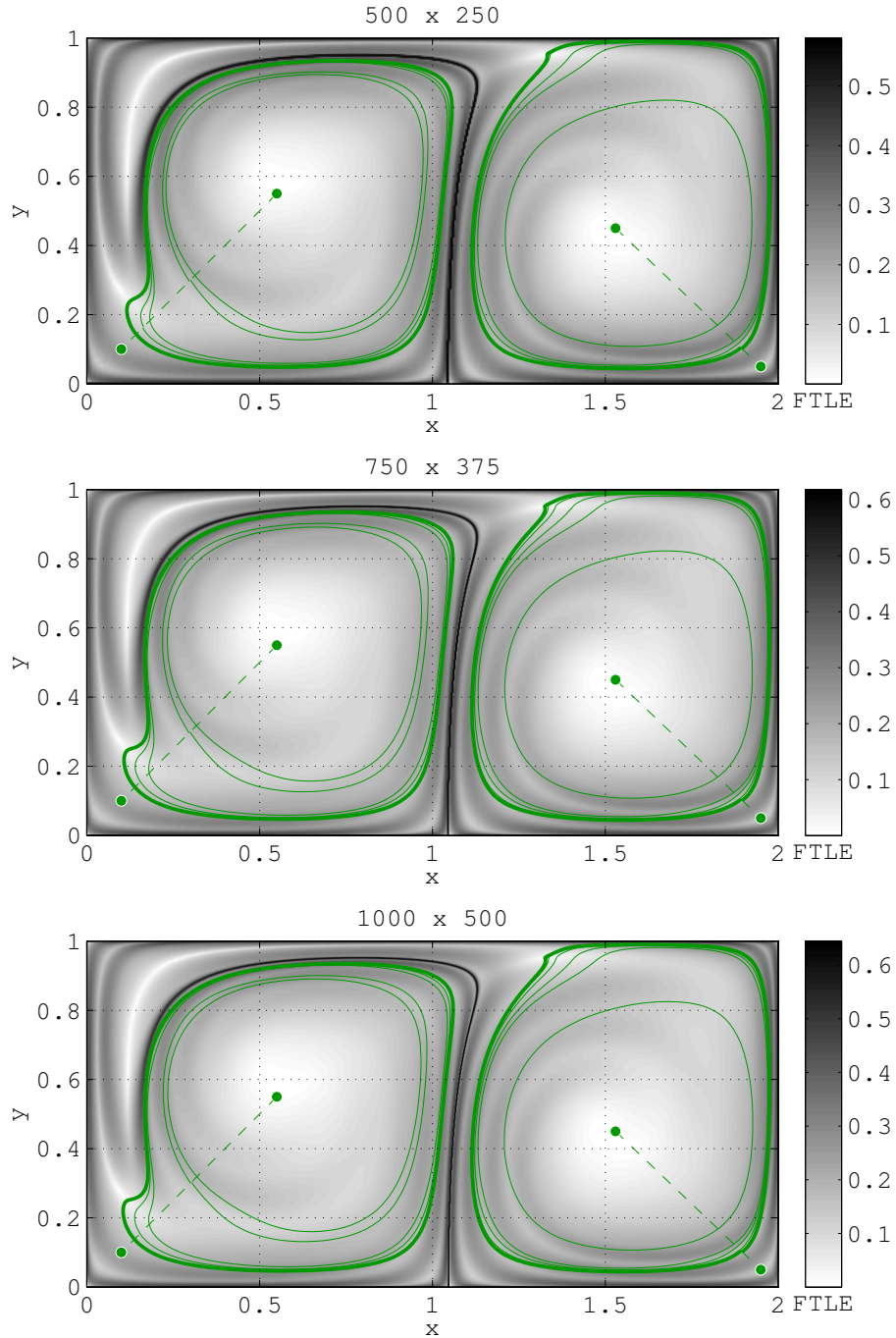


Figure 5: Convergence of closed λ -lines for increasing main-grid resolution in the double-gyre model. The outermost closed λ -line (bold green line) is the vortex boundary. (Top) [500x250], λ -values of closed orbits from interior to exterior, left gyre: $\lambda = (0.97, 0.98, 0.99, 1.00, 1.01)$, right gyre: $\lambda = (1.00, 1.01, 1.02, 1.03, 1.04)$; (Middle) [750x375], left: $\lambda = (0.97, 0.98, 0.99, 1.00, 1.01)$, right: $\lambda = (1.00, 1.01, 1.02, 1.03, 1.04, 1.05)$; (Bottom) [1000x500], left: $\lambda = (0.97, 0.98, 0.99, 1.00, 1.01)$, right: $\lambda = (1.00, 1.01, 1.02, 1.03, 1.04, 1.05)$.

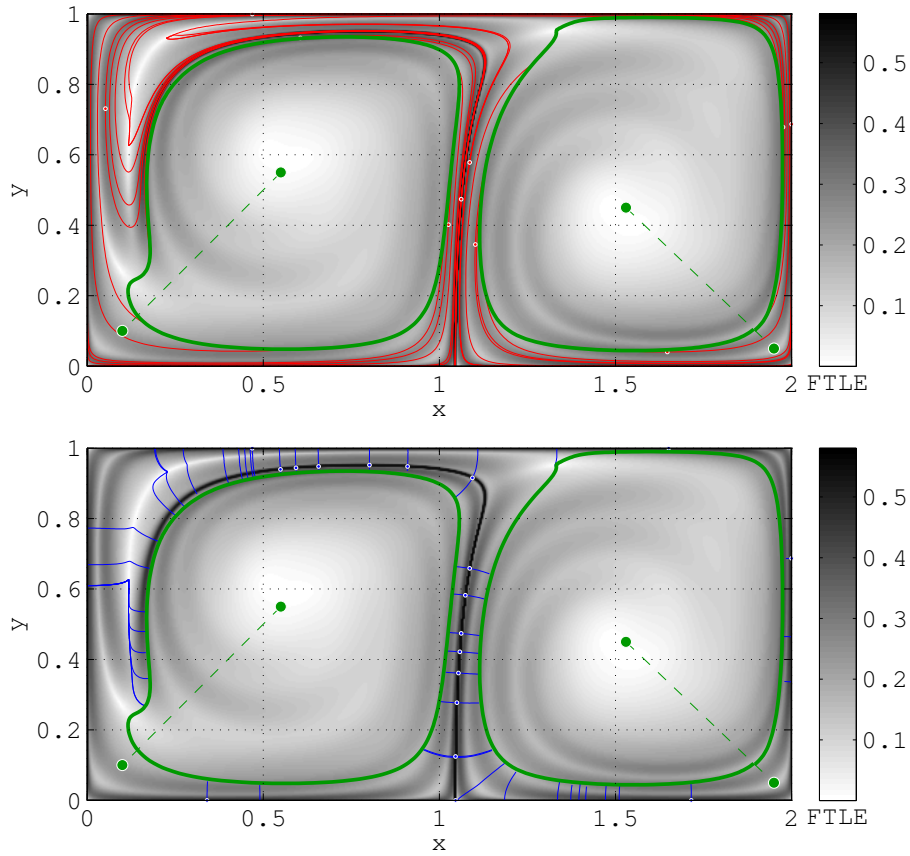


Figure 6: LCSs in the double gyre flow. Resolution $[500 \times 250]$. $\lambda = 1.00$ and 1.04 for the left and the right gyre. $\lambda \in [0.93, 1.07]$, $\Delta\lambda = 0.01$. (Top) Elliptic (green) and repelling (red) LCSs with the FTLE shown in the background. (Bottom) Elliptic and attracting (blue) LCSs.

4.2 Bickley jet

The Bickley jet models a meandering zonal jet flanked above and below by counter-rotating vortices. This is an idealized model of geophysical flows such as the Gulf Stream or the polar night jet perturbed by a Rossby wave [8, 3].

The velocity is given by $v(x, y, t) = (-\partial_y \psi, \partial_x \psi)$ where

$$\begin{aligned}\psi(x, y, t) &= \psi_0(x, y) + \psi_1(x, y, t), \\ \psi_0(x, y) &= c_3 y - UL_y \tanh \frac{y}{L_y} + \epsilon_3 UL_y \operatorname{sech}^2 \frac{y}{L_y} \cos k_3 x, \\ \psi_1(x, y, t) &= UL_y \operatorname{sech}^2 \frac{y}{L_y} \operatorname{Re} \left[\sum_{n=1}^2 \epsilon_n f_n(t) e^{ik_n x} \right].\end{aligned}$$

As a forcing function, we choose a solution running on the chaotic attractor of the damped-forced Duffing oscillator. Specifically, we let

$$\begin{aligned}\frac{d\phi_1}{dt} &= \phi_2, \\ \frac{d\phi_2}{dt} &= -0.1\phi_2 - \phi_1^3 + 11 \cos(t), \\ f_{1,2}(t) &= 2.625 \times 10^{-2} \phi_1(t/6.238 \times 10^5).\end{aligned}$$

The parameter values we use are: $U = 62.66$, $c_2 = 0.205U$, $c_3 = 0.461U$, $L_y = 1.77 \times 10^6$, $\epsilon_1 = 0.0075$, $\epsilon_2 = 0.04$, $\epsilon_3 = 0.3$, $L_x = 6.371 \times 10^6 \pi$, $k_n = 2n\pi/L_x$, $\sigma_1 = 0.5k_2(c_2 - c_3)$, $\sigma_2 = 2\sigma_1$.

The integration time is $T = 4L_x/U$, a multiple of the eddy turnover time in the flow (see also LCS Tool file `flow_animation.m`). Listing 4 shows the code of LCS Tool in which the chaotically perturbed velocity field is defined (ll. 11-18), the boundaries are set to periodic in the x-direction (l. 20), and five Poincare sections are defined where we expect coherent vortices (ll. 46-50). λ -values for the closed orbit detection are varied over the range $[0.80, 1.20]$ with a step of 0.01.

Figure 7 shows elliptic and hyperbolic LCSs of the Bickley jet with the FTLE field in the background.

```

%% Input parameters
2  u = 62.66;
   lengthX = pi*earthRadius;
4  lengthY = 1.77e6;
   epsilon = [.075,.4,.3];
6  domain = [0,lengthX;[-1,1]*2.25*lengthY];
   resolutionX = 500;
8  timespan = [0,4*lengthX/u];

10 %% Velocity definition
   perturbationCase = 3;
12 phiTimespan = [0,25];

```

```

phiInitial = [0,0];
14 phiSol = ode45(@d_phi,phiTimespan,phiInitial);
timeResolution = 1e5;
16 phi1 = deval(phiSol,linspace(phiTimespan(1),phiTimespan(2),timeResolution),1)
;
phi1Max = max(phi1);
18 lDerivative = @(t,x,~)derivative(t,x,false,u,lengthX,lengthY,epsilon,
perturbationCase,phiSol,phi1Max);
incompressible = true;
20 periodicBc = [true,false];

22 %% Cauchy–Green strain eigenvalues and eigenvectors
[cgEigenvector,cgEigenvalue] = eig_cgStrain(lDerivative,domain,resolution,
timespan,'incompressible',incompressible);

24
%% LCS parameters
26 % Lambda–lines
lambdaStep = 0.01;
28 lambdaRange = 0.80:lambdaStep:1.10;
lambdaLineOdeSolverOptions = odeset('relTol',1e-6);

30
% Shrinklines
32 shrinklineMaxLength = 1e8;
shrinklineLocalMaxDistance = 8*gridSpace;
34 shrinklineOdeSolverOptions = odeset('relTol',1e-4);

36 % Stretchlines
stretchlineMaxLength = 1e8;
38 stretchlineLocalMaxDistance = 4*gridSpace;
stretchlineOdeSolverOptions = odeset('relTol',1e-4);

40
%% Lambda–line LCSs
42 % Define Poincare sections; first point in center of elliptic region and
% second point outside elliptic region
44 poincareSection = struct('endPosition', {}, 'numPoints', {}, 'orbitMaxLength', {});

46 poincareSection(1).endPosition = [3.25e6, 1.5e6; 1.4e6, 2.6e6];
poincareSection(2).endPosition = [6.50e6, -1.4e6; 5.0e6, -3.0e6];
48 poincareSection(3).endPosition = [1.0e7, 1.5e6; 8.0e6, 2.6e6];
poincareSection(4).endPosition = [1.35e7, -1.4e6; 1.5e7, -0.5e6];
50 poincareSection(5).endPosition = [1.65e7, 1.5e6; 1.5e7, 2.6e6];

52 % Number of orbit seed points along each Poincare section
[poincareSection.numPoints] = deal(80);

54
% Set maximum orbit length to twice the expected circumference
56 nPoincareSection = numel(poincareSection);
for i = 1:nPoincareSection
58 rOrbit = hypot(diff(poincareSection(i).endPosition(:,1)),diff(poincareSection
(i).endPosition(:,2)));

```

```

    poincareSection(i).orbitMaxLength = 2*(2*pi*rOrbit);
60 end
62 ...
    for lambda = lambdaRange
64 ...
        [shearline.etaPos,shearline.etaNeg] = lambda_line(CG_Eigenvector,
            CG_Eigenvalue,lambda);
66 closedLambdaLineCandidate = poincare_closed_orbit_multi(domain,
            resolution,shearline,poincareSection,'odeSolverOptions',
            lambdaLineOdeSolverOptions);
        ...
68 end
        ...
70 %% Hyperbolic shrinkline LCSs
        [shrinklineLcs,shrinklineLcsInitialPosition] = seed_curves_from_lambda_max(
            shrinklineLocalMaxDistance,shrinklineMaxLength,CG_Eigenvalue(:,2),
            CG_Eigenvector(:,1:2),domain,resolution,'periodicBc',periodicBc,'
            odeSolverOptions',shrinklineOdeSolverOptions);
72
74 %% Hyperbolic stretchline LCSs
        [stretchlineLcs,stretchlineLcsInitialPosition] = seed_curves_from_lambda_max(
            stretchlineLocalMaxDistance,stretchlineMaxLength,-CG_Eigenvalue(:,1),
            CG_Eigenvector(:,3:4),domain,resolution,'periodicBc',periodicBc,'
            odeSolverOptions',stretchlineOdeSolverOptions);

```

Listing 4: Bickley jet script for hyperbolic and elliptic LCSs.

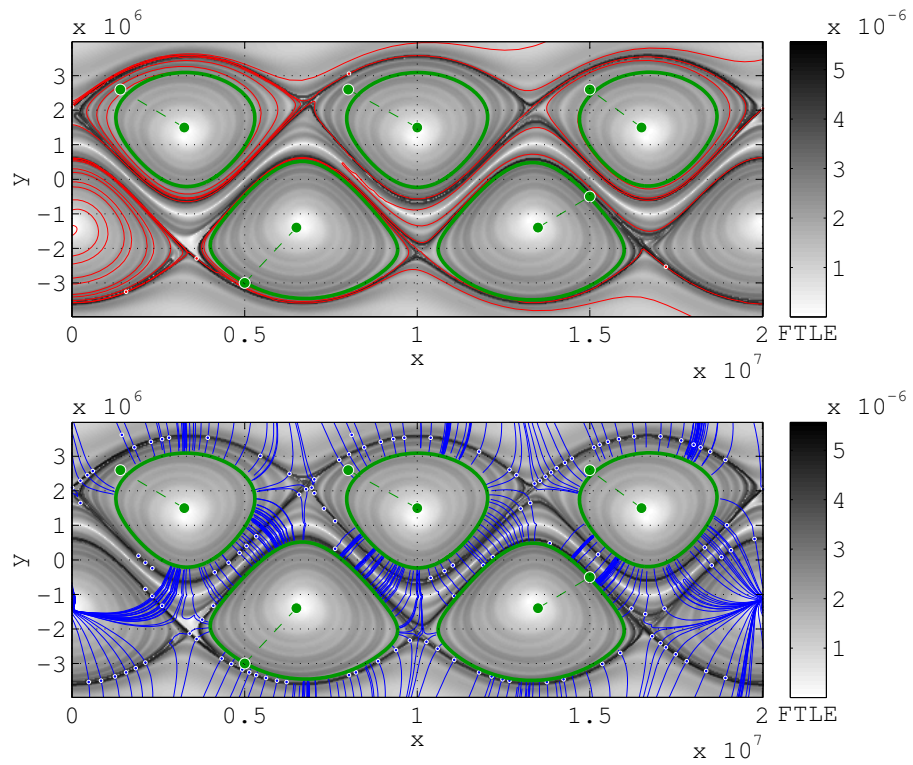


Figure 7: Elliptic and hyperbolic (top: red - repelling, bottom: blue - attracting) LCSs in the Bickley jet. λ -valuestrains of coherent eddies from left to right $[0.95, 0.80, 0.94, 0.80, 0.94]$, $\lambda \in [0.80, 1.20]$, $\Delta\lambda = 0.01$.

4.3 Ocean velocity data from satellite altimetry

This last example demonstrates the use of LCS Tool on velocity data derived from satellite-observed sea-surface heights under the geostrophic approximation. In contrast to the previous two analytic examples, the velocity field is available only with discrete temporal and spatial resolution. Our region of interest is a small domain in the South Atlantic Ocean, where exceptionally coherent eddies (Agulhas rings) were recently found by [19] using the theory we surveyed in Section 2.1.

In the geostrophic approximation, the sea-surface height η serves as a stream-function for surface velocities. In a longitude-latitude (φ, θ) coordinate system, the evolution of a fluid particle is given by

$$\dot{\varphi}(\varphi, \theta, t) = -\frac{g}{R^2 f(\theta) \cos \theta} \partial_{\theta} \eta(\varphi, \theta, t) \quad (9)$$

$$\dot{\theta}(\varphi, \theta, t) = +\frac{g}{R^2 f(\theta) \cos \theta} \partial_{\varphi} \eta(\varphi, \theta, t) \quad (10)$$

where g is the constant of gravity, R is the mean radius of the Earth, and $f(\theta) \equiv 2\Omega \sin \theta$ is the Coriolis parameter, with Ω denoting the Earth's mean angular velocity.

The data is given at a spatial resolution of $1/4^\circ$ and a temporal resolution of 7 days. Due to the discrete data, defining the right-hand side of Equation (9) and (10) involves spline interpolation in space and time. An interpolant is generated first, then the function `flowdata.derivative` evaluates the interpolants for the zonal and meridional velocity at the needed coordinates. Listing 5 shows the relevant part of the code in LCS Tool's ocean demo file `hyperbolic_shear_lcs.m`. In lines 8-11, the commands for the interpolation of the velocity data set are given.

```

2  % Input parameters
3  domain = [0,6;-34,-28];
4  resolution = [400,400];
5  timespan = [100,130];
6
7  % Velocity definition
8  load('ocean_geostrophic_velocity.mat');
9  ...
10 interpMethod = 'spline';
11 vlon_interpolant = griddedInterpolant({time,lat,lon},vlon,interpMethod);
12 vlat_interpolant = griddedInterpolant({time,lat,lon},vlat,interpMethod);
13 lDerivative = @(t,x,~)flowdata.derivative(t,x,vlon_interpolant,vlat_interpolant);
14 incompressible = true;
15
16 % LCS parameters
17 % Cauchy-Green strain
18 cgEigenvalueFromMainGrid = false;
19 cgAuxGridRelDelta = 0.01;

```



```

20 % Lambda-lines
    lambdaStep = 0.02; lambdaRange = 0.90:lambdaStep:1.10;
22 lambdaLineOdeSolverOptions = odeset('relTol',1e-6);

24 % Shrinklines
    shrinklineMaxLength = 20;
26 gridSpace = diff(domain(1,:))/(double(resolution(1))-1);
    shrinklineLocalMaxDistance = 2*gridSpace;
28 shrinklineOdeSolverOptions = odeset('relTol',1e-4);

30 % Stretchlines
    stretchlineMaxLength = 20;
32 stretchlineLocalMaxDistance = 4*gridSpace;
    stretchlineOdeSolverOptions = odeset('relTol',1e-4);
34 ...
    % Cauchy-Green strain eigenvalues and eigenvectors
36 [cgEigenvector,cgEigenvalue] = eig_cgStrain(IDerivative,domain,resolution,
        timespan,'incompressible',incompressible,'eigenvalueFromMainGrid',
        cgEigenvalueFromMainGrid,'auxGridRelDelta',cgAuxGridRelDelta);

38 % Lambda-line LCSs
    % Define Poincare sections; ...
40 poincareSection = struct('endPosition',{},'numPoints',{},'orbitMaxLength',{});
    ...
42 poincareSection(1).endPosition = [3.3,-32.1;3.7,-31.6];
    poincareSection(2).endPosition = [1.3,-30.9;1.9,-31.1];
44
    % Number of orbit seed points along each Poincare section
46 [poincareSection.numPoints] = deal(100);

48 % Set maximum orbit length to twice the expected circumference
    nPoincareSection = numel(poincareSection);
50 for i = 1:nPoincareSection
        rOrbit = hypot(diff(poincareSection(i).endPosition(:,1)),diff(poincareSection
            (i).endPosition(:,2)));
52     poincareSection(i).orbitMaxLength = 2*(2*pi*rOrbit);
    end
54
    for lambda = lambdaRange
56     ...
        [shearline.etaPos,shearline.etaNeg] = lambda_line(cgEigenvector,
            cgEigenvalue,lambda);
58     closedLambdaLineCandidate = poincare_closed_orbit_multi(domain,
        resolution,shearline,poincareSection,'odeSolverOptions',
        lambdaLineOdeSolverOptions,'showGraph',showGraph);
        ...
60     end
        ...
62 % Hyperbolic shrinkline LCSs

```

```

shrinklineLcs = seed_curves_from_lambda_max(shrinklineLocalMaxDistance,
shrinklineMaxLength,cgEigenvalue(:,2),cgEigenvector(:,1:2),domain,
resolution,'odeSolverOptions',shrinklineOdeSolverOptions);
64 ...
% Hyperbolic stretchline LCSs
66 stretchlineLcs = seed_curves_from_lambda_max(stretchlineLocalMaxDistance,
stretchlineMaxLength,-cgEigenvalue(:,1),cgEigenvector(:,3:4),domain,
resolution,'odeSolverOptions',stretchlineOdeSolverOptions);

```

Listing 5: LCS Tool demo script to compute LCS from an ocean data set.

We choose the integration time as $T = 30$ days (Listing 5, l. 4), which is larger than the eddy turnover time in this region. The resolution of the main computational grid for initial conditions is set to 400×400 (l. 3). This corresponds to a resolution of roughly 0.015° and gives good results. With this choice, the resolution of the tracer grid is 15 times higher than the resolution of the velocity field. The flow is integrated and the Cauchy-Green strain tensor is computed by the function `eig_cgStrain` (l. 35). Incompressibility of the flow is enforced (l. 12), the auxiliary grid distance is set to 1% of the main grid distance (l. 17), and eigenvalues are computed from the auxiliary grid (l. 16). Elliptic LCSs are computed in line 54, after the Poincare sections have been set (ll. 41-42) and the η_{\pm}^{λ} fields have been defined (l. 53). λ -values are varied over a range of $[0.90, 1.10]$ with a step of 0.02 (l. 20). Hyperbolic LCSs are computed in lines 57 and 59.

Figure 8 shows the positions of elliptic and hyperbolic LCSs on 22 November 2006, which is the same time instant analyzed in [19, 4]. Here the integration time is chosen as $T = 30$ days, as opposed to 90 days in the cited references, to avoid the length tangling of hyperbolic LCSs. Our analysis via LCS Tool reveals five coherent eddy boundaries. The large coherent eddy at $(3, -32)$ has a non-stretching boundary, i.e., $\lambda = 1.00$. It corresponds to eddy #2 in Figure 3 of [4]. Additionally, four further smaller coherent eddy cores are found. They do not stay coherent over a time of 90 days. All closed orbits are stable under increased spatial resolution for the Cauchy-Green strain tensor field. Repelling LCSs (red) and attracting LCSs (blue) are superimposed over the plot of FTLE values. The hyperbolic LCSs determine the deformation of the fluid in-between coherent eddy cores.

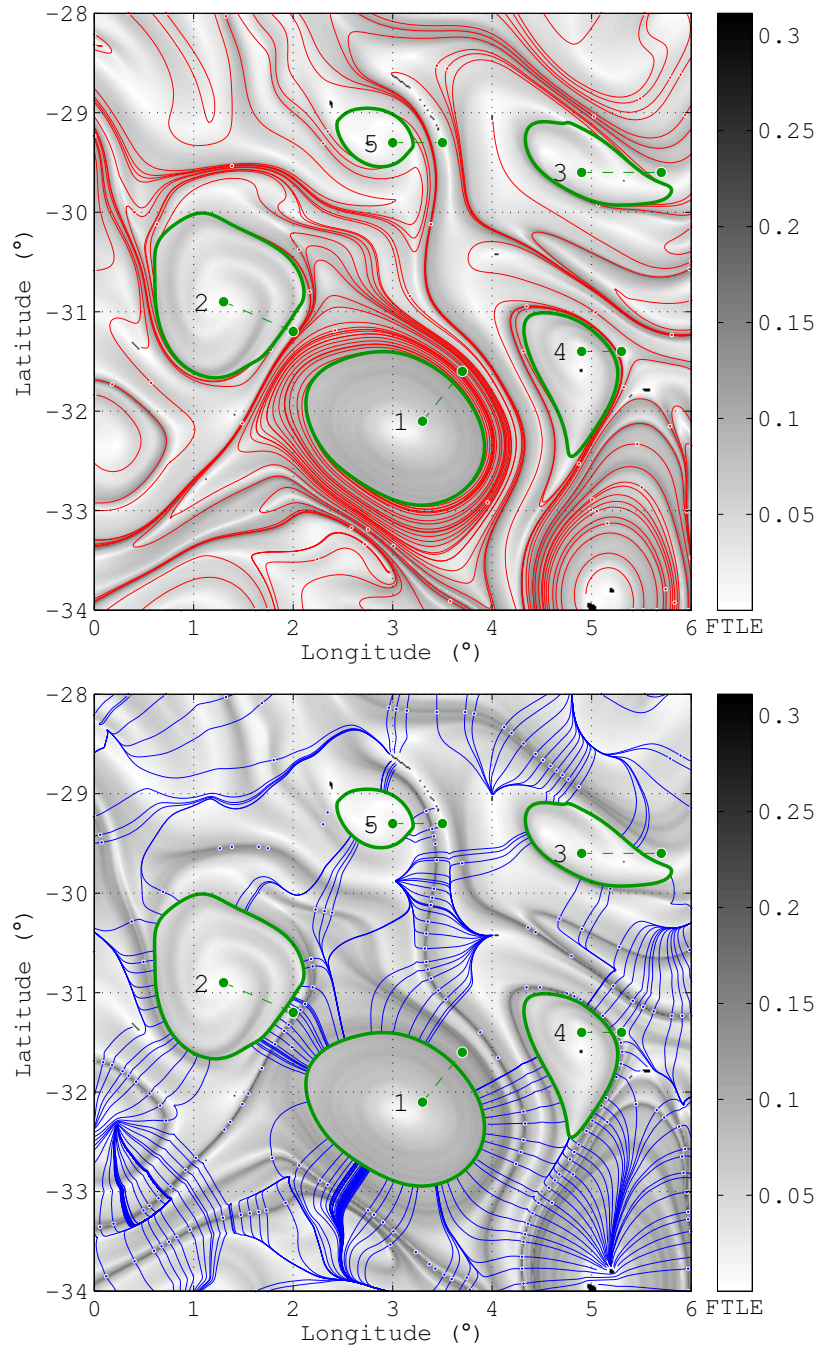


Figure 8: (Top) Elliptic LCSs (green, $\lambda = 1.00, 1.08, 0.94, 0.90, 1.06$) and repelling LCSs (red) in the ocean data set. Background gray-scale is the finite time Lyapunov exponent. Dashed green lines are Poincaré sections. White dots indicate λ_2 local maxima used as initial positions for shrinkline integration. (Bottom) Elliptic LCSs (green) and attracting LCSs (blue).

5 Conclusions

We have described a computational toolbox, LCS Tool, that implements recent variational results for Lagrangian Coherent Structures (LCSs) in two-dimensional unsteady flows. We have also demonstrated the performance of LCS Tool on two analytic flow models and a geophysical velocity dataset. The publicly available software library producing these results enables the exploration of variational LCS methods without assuming a detailed knowledge of geodesic LCS theory.

LCS Tool leverages the capabilities of MATLAB extensively. For FTLE-based extraction of LCSs, computational performance has received considerable attention [6, 25]. We hope to see similar computational advances for the publicly available LCS Tool platform. Optimizing computational performance will likely aid the application of variational LCS methods to large-scale real-time forecasting applications, such as the tracking of environmental contaminants [27].

We also hope that LCS Tool will serve as a foundation for the numerical implementation of recent theoretical advances. These include the geodesic theory of parabolic LCSs (jet cores) [12] and the variational theory of hyperbolic and elliptic LCSs for three-dimensional flows [5].

Acknowledgments

The altimeter products used in this work are produced by SSALTO/DUACS and distributed by AVISO, with support from CNES <http://www.avisooceanobs.com/duacs>

References

- [1] S. Ali and M. Shah. A Lagrangian Particle Dynamics Approach for Crowd Flow Segmentation and Stability Analysis. *IEEE International Conference on Computer Vision and Pattern Recognition (CVPR)*, 2007.
- [2] V.I. Arnold. *Mathematical methods of classical mechanics*. Springer-Verlag, 1978.
- [3] F.B. Beron-Vera, M.J. Olascoaga, M.G. Brown, H. Koçak, and I.I. Rypina. Invariant-tori-like Lagrangian coherent structures in geophysical flows. *Chaos*, 20:017514, 2010. doi: 10.1063/1.3271342.
- [4] F.J. Beron-Vera, Y. Wang, M.J. Olascoaga, G. Goni, and G. Haller. Objective detection of oceanic eddies and the Agulhas leakage. *J. Phys. Ocean.*, 2013. doi: 10.1175/JPO-D-12-0171.1.
- [5] D. Blazevski and G. Haller. Hyperbolic and elliptic transport barriers in three-dimensional unsteady flows. *Physica D*, 273–274:46–62, 2014.

- [6] C. Conti, D. Rossinelli, and P. Koumoutsakos. GPU and APU computations of Finite Time Lyapunov Exponent fields. *J. Comp. Phys.*, 231(5): 2229–2244, 2012. doi: 10.1016/j.jcp.2011.10.032.
- [7] J. O. Dabiri. LCS MATLAB Kit, 2009. URL <http://dabiri.caltech.edu/software.html>.
- [8] D. del Castillo-Negrete and P. J. Morrison. Chaotic transport by Rossby waves in shear flow. *Phys. Fluids A*, 5(4):948–965, 1993.
- [9] T. Delmarcelle and L. Hesselink. The topology of symmetric, second-order tensor fields. In *Visualization, 1994., Visualization '94, Proceedings., IEEE Conference on*, pages 140–147, 10 1994. doi: 10.1109/VISUAL.1994.346326.
- [10] P.C. du Toit. *Transport and separatrices in time-dependent flows*. PhD thesis, California Institute of Technology, 2010. URL <http://resolver.caltech.edu/CaltechTHESIS:10072009-165901284>.
- [11] M. Farazmand and G. Haller. Computing Lagrangian coherent structures from their variational theory. *Chaos*, 22(1), 2012. doi: 10.1063/1.3690153.
- [12] M. Farazmand, D. Blazevski, and G. Haller. Shearless transport barriers in unsteady two-dimensional flows and maps. *Physica D*, 278-279:44–57, 2014.
- [13] E.S. Gawlik, J.E. Marsden, P.C. Du Toit, and S. Campagnola. Lagrangian coherent structures in the planar elliptic restricted three-body problem. *Celest. Mech. Dyn. Astr.*, 103:227–249, 2009.
- [14] A. Hadjighasem, M. Farazmand, and G. Haller. Detecting invariant manifolds, attractors, and generalized KAM tori in aperiodically forced mechanical systems. *Nonlinear Dynamics*, 73(1-2):689–704, 2013. ISSN 0924-090X. doi: 10.1007/s11071-013-0823-x.
- [15] G. Haller. Distinguished material surfaces and coherent structures in three-dimensional fluid flows. *Physica D*, 149:248–277, 2001.
- [16] G. Haller. A variational theory of hyperbolic Lagrangian Coherent Structures. *Physica D*, 240(7):574–598, 3 2011. doi: 10.1016/j.physd.2010.11.010.
- [17] G. Haller. Lagrangian coherent structures. *Ann. Rev. Fluid Mech.* (to appear), 2014.
- [18] G. Haller and F.J. Beron-Vera. Geodesic Theory of Transport Barriers in Two-Dimensional Flows. *Physica D*, 241(20):1680–1702, 10 2012. doi: 10.1016/j.physd.2012.06.012.
- [19] G. Haller and F.J. Beron-Vera. Coherent Lagrangian vortices: the black holes of turbulence. *J. Fluid Mech.*, 731:R4, 2013. doi: 10.1017/jfm.2013.391.

- [20] G. Haller and G. Yuan. Lagrangian coherent structures and mixing in two-dimensional turbulence. *Physica D*, 147:352–370, 2000.
- [21] F. Huhn, A. von Kameke, V. Pérez-Muñuzuri, M.J. Olascoaga, and F.J. Beron-Vera. The impact of advective transport by the South Indian Ocean Countercurrent on the Madagascar plankton bloom. *Geophys. Res. Lett.*, 39:L06602, 2012.
- [22] D. Karrasch, F. Huhn, and G. Haller. Automated detection of coherent Lagrangian vortices in two-dimensional unsteady flows. *submitted*, 2014.
- [23] T.-Y. Koh and B. Legras. Hyperbolic lines and the stratospheric polar vortex. *Chaos*, 12(2):382–394, 2002.
- [24] F. Lekien. *Time-dependent dynamical systems and geophysical flows*. PhD thesis, California Institute of Technology, 2003. URL <http://resolver.caltech.edu/CaltechETD:etd-04082003-180353>.
- [25] P. Miron, J. Vétel, A. Garon, M. Delfour, and M. El Hassan. Anisotropic mesh adaptation on Lagrangian Coherent Structures. *J. Comp. Phys.*, 231(19):6419–6437, 2012. doi: 10.1016/j.jcp.2012.06.015.
- [26] G. Norgard and P.-T. Bremer. Second derivative ridges are straight lines and the implications for computing Lagrangian Coherent Structures. *Physica D*, 241(18):1475–1476, 9 2012. ISSN 0167-2789. doi: 10.1016/j.physd.2012.05.006.
- [27] M. J. Olascoaga and G. Haller. Forecasting sudden changes in environmental pollution patterns. *Proc. Nat. Acad. Sci.*, 109(13):4738–4743, 2012.
- [28] T. Peacock and G. Haller. Lagrangian coherent structures: The hidden skeleton of fluid flows. *Physics Today*, 66(2):41–47, 2013. doi: 10.1063/PT.3.1886.
- [29] S.C. Shadden. FlowVC, 2010. URL <http://shaddenlab.berkeley.edu/software.html>.
- [30] S.C. Shadden, F. Lekien, and J.E. Marsden. Definition and properties of Lagrangian coherent structures from finite-time Lyapunov exponents in two-dimensional aperiodic flows. *Physica D*, 212(3-4):271–304, 12 2005. doi: 10.1016/j.physd.2005.10.007.
- [31] P. Tallapragada, S.D. Ross, and D.G. Schmale III. Lagrangian coherent structures are associated with fluctuations in airborne microbial populations. *Chaos*, 21(3):033122, 2011. doi: 10.1063/1.3624930.
- [32] W. Tang, P.W. Chan, and G. Haller. Accurate extraction of Lagrangian coherent structures over finite domains with application to flight data analysis over Hong Kong International Airport. *Chaos*, 20(1):017502, 2010. doi: 10.1063/1.3276061.

- [33] C. Truesdell and W. Noll. *The Non-Linear Field Theories of Mechanics*. Springer, 2004.
- [34] M.M. Wilson, J. Peng, J.O. Dabiri, and J.D. Eldredge. Lagrangian coherent structures in low Reynolds number swimming. *J. Phys.: Condens. Mat.*, 21(20):204105, 2009. doi: 10.1088/0953-8984/21/20/204105.